Journal of
Synchrotron
Radiation

ISSN 0909-0495

Received 8 September 2008
Accepted 10 February 2009

Quality evaluation of quick-frozen biological specimens by simultaneous microbeam SAXS/WAXS recordings

Hiroyuki Iwamoto

Research and Utilization Division, SPring-8, Japan Synchrotron Radiation Research Institute, Hyogo 679-5198, Japan. E-mail: iwamoto@spring8.or.jp

The quality of small-angle X-ray scattering (SAXS) patterns from quick-frozen hydrated biological specimens was correlated with the extent of ice crystal formation by simultaneously recording wide-angle X-ray scattering (WAXS) of ice, at a micrometer-order spatial resolution by using X-ray microbeams. Flight muscle fibers from a giant waterbug, *Lethocerus*, known to generate well defined small-angle reflection spots originating from the hexagonal lattices of myofilaments, were quick-frozen in the presence or absence of various cryoprotectants. Freezing without a cryoprotectant resulted in massive ice-crystal formation at almost all depths of the specimen, and the occurrence of reflection spots was limited to the region close to the specimen surface. Inclusion of 20% dimethyl sulfoxide or methylpentanediol ensured ideal vitreous ice formation and good diffraction qualities for up to 100 μm from the specimen surface. Glycerol and sucrose were found to be inferior at a 20% concentration, but left the reflection spots observable at depths of up to 100 μm. Thus, the microbeam SAXS/WAXS recording offers a high-spatial-resolution means of evaluating the extent of structure preservation of quick-frozen biological specimens. The technique presented here may also provide useful information in cryoelectron microscopy.

Keywords: microbeam; SAXS/WAXS recording; ice crystals; liquid-nitrogen temperature.

1. Introduction

The small scattering cross section of materials for X-ray beams had long defined the lower limit of the size of specimens for diffraction/scattering studies, but this limitation has been removed by evolving third-generation synchrotron radiation sources and improving techniques to generate and use X-ray microbeams. Diffraction techniques using X-ray microbeams (microdiffraction) have wide applications in polymer and biopolymer science (for reviews, see Riekel *et al.*, 2003; Riekel & Davies, 2005), and recently they have also been applied to hydrated non-crystalline biological specimens, which are more unstable and more susceptible to radiation damage than dry polymers. In an earlier study (Iwamoto *et al.*, 2002), raw hydrated biological specimens were used (myofibrils from insect flight muscle), but it has been demonstrated that quick freezing of hydrated biological specimens greatly increases their stability and resistance to radiation damage (Iwamoto *et al.*, 2005). Microdiffraction of frozen hydrated biological specimens is finding applications in the fields of evolutionary (Iwamoto *et al.*, 2006) and developmental (Iwamoto *et al.*, 2007) biology.

For diffraction studies of frozen hydrated biological specimens, it is essential to prevent the formation of ice crystals, which destroy the fine structure of specimens. From electron microscopic studies, it is known that the fine structure of specimens is preserved in amorphous (vitreous) ice, which is generated and retained only if the specimen is cooled rapidly and kept below the transition temperature (∼140 K) for the vitreous and crystalline phases (for a review, see *e.g.* Barnard, 1987).

The prevention of ice crystal formation has also become a major interest among protein crystallographers since it became a common practice to flash-cool protein crystals in a flow of cooled nitrogen gas or by other means, and several extensive studies have been published concerning the relation between the extent of ice crystal formation and the kind and concentration of cryoprotectants, the volume of the liquid drop, cooling rate *etc.* (*e.g.* Warkentin *et al.*, 2006). Among others, Berejnov *et al.* (2006) have clearly demonstrated that in the flash-cooled liquid drops containing various cryoprotectants the diffuse X-ray scattering of ice that peaked at a *d*-spacing of 3.7 Å is transformed into a series of sharp peaks as the ice quality deteriorates from the vitreous state to cubic and

then hexagonal crystalline states. A similar electron-microscopy-oriented study has also been conducted for the effect of sucrose (Lepault *et al.*, 1997).

In these studies the quality of ice has been determined for liquid drops as a whole. However, it is expected that the surface of a specimen is cooled at a greater rate than its core, resulting in better preservation of fine structure with lower concentrations of cryoprotectants. Therefore it would be informative to determine the relation between the depth from the surface of the specimen, the state of the ice and the quality of diffraction from the specimen. This information would be particularly useful in microdiffraction studies in which a better-preserved volume of the specimen can be targeted with fine-focused microbeams. Here we describe the method to simultaneously record small-angle diffraction patterns from specimens and wide-angle scattering profiles from ice by using X-ray microbeams, and provide examples of results from the flight muscle of a giant waterbug, *Lethocerus*, which was frozen in the presence or absence of various cryoprotectants. The information described here is expected to be beneficial in developing better methods for quick freezing, not only for X-ray diffraction from non-crystalline hydrated biological materials but also for cryocrystallography and electron microscopy.

2. Materials and methods

2.1. Materials

The flight muscle fibers of a giant waterbug were obtained from a reared specimen of *Lethocerus deyrollei*. The fibers had been stored in a 75%:25% mixture of glycerol and a relaxing solution (for composition, see Iwamoto, 1995) for one year in a deep freezer at 188 K (Tregear *et al.*, 1998). Before freezing, the fibers were transferred to a rigor solution (for composition, see Iwamoto, 2000) containing various cryoprotectants. Pieces of fibers (length $\sim$2 mm, diameter $\sim$200 µm) were then mounted on brass rods (1 mm $\times$ 2 mm in cross section) with pieces of paper attached on top, quick-frozen by plunging into liquid propane ($\sim$93 K), trimmed to a length of $\sim$500 µm to remove deformed ends (Fig. 1*c*) and stored in liquid nitrogen until use as described previously (Iwamoto *et al.*, 2006). As a plunging mechanism, a commercial device for immersion freezing (Leica CPC) was used, following instructions from the manufacturer. The brass rod was fitted to a pre-cooled lathe-machined copper block, which was designed to easily fit to the specimen holder of the cryochamber (Figs. 1*a* and 1*b*).

2.2. Measurement of cooling rate

The cooling rate of the specimen was measured by placing a fine-gauge thermocouple junction formed between 13 µm alumel and chromel wires (Omega Thermo, model CHAL-0005) at the position of the specimen on the brass rod, and by plunging it into liquid propane cooled to 99 K. The signal was amplified by a thermocouple conditioner (AD597AH, Analog Devices), digitized and stored on a personal computer by using an analog-to-digital converter built in-house at a conversion rate of 2500 conversions per second.

2.3. Cryochamber

The specimens were kept at $\sim$70 K during exposure to X-ray microbeams in an in-vacuum cryochamber. The cryo-

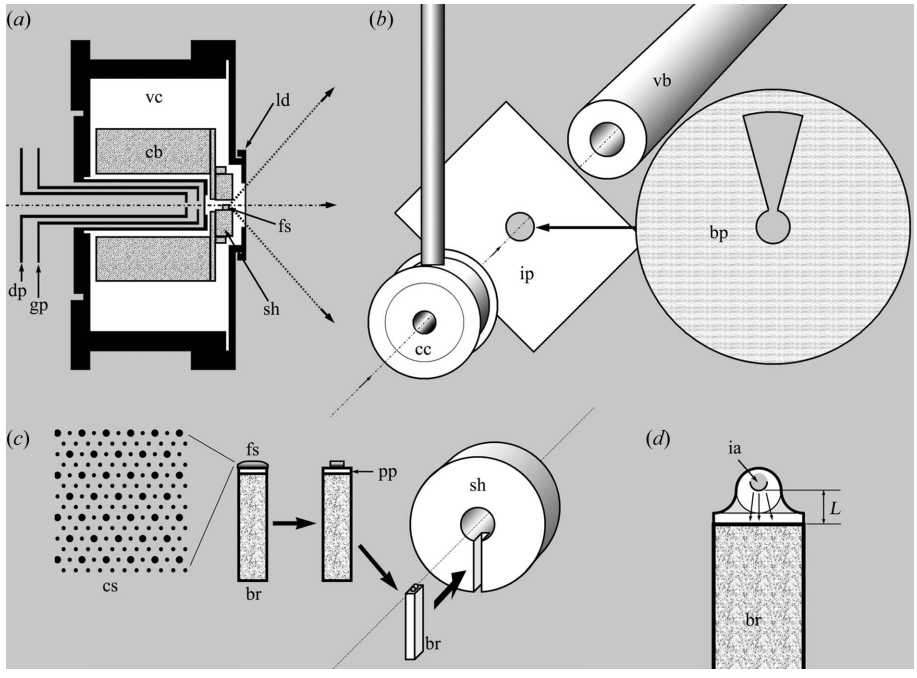

Figure 1
Set-up for microbeam SAXS/WAXS measurements of frozen biological samples. (*a*) Schematic diagram of the cross section of the modified cryochamber. cb, cooled block; dp, super-invar tubing with the defining pinhole on top; fs, frozen sample; gp, super-invar tubing with the guard pinhole on top; ld, lid for specimen exchange; sh, specimen holder made of copper; vc, vacuum chamber. Upstream is on the left-hand side of the drawing. (*b*) Schematic diagram of the arrangement of components. bp, brass plate to cover the imaging plate except for the fan-shaped opening; cc, cryochamber; ip, cassette for the imaging plate attached to a motorized rotating stage on its back (not drawn); vb, vacuum beam path leading to the SAXS detector. (*c*) Method of adapting a specimen-bearing brass rod to the specimen holder. The specimen is a flight muscle fiber or fiber bundles, initially $\sim$2 mm in length and $\sim$200 µm in diameter. In its cross section, myofilamens are arranged in a hexagonal lattice with a unit-cell size of $\sim$45 nm. After freezing, this specimen is trimmed to leave a central straight segment of $\sim$500 µm in length. br, brass rod; cs, cross section; pp, piece of paper. (*d*) Diagram for heat transfer from the irradiated area of the specimen (shaded circle) to the brass rod, which is kept at $\sim$70 K and serves as a heat sink. This geometry is used to estimate the thermal effect of microbeam irradiation (see Appendix *A*). It is assumed that the effective surface of heat conduction is half of the surface area of the irradiated volume (black arc). It is also assumed that the distance between the irradiated area and the brass rod (L) is 500 µm and that the space between them is filled with ice. The arrows indicate the flow of heat. ia, irradiated area.

chamber was of low-drift type (Microstat He HiRes II; Oxford Instruments), which had submicrometer positional stability without the need of an externally attached drift-compensating mechanism (see Iwamoto *et al.*, 2006). Its specimen holder had been modified to accommodate the frozen specimens mounted on brass blocks. The upstream and downstream lids had also been replaced with ones with Kapton windows to allow incident and diffracted X-rays. The lids were also designed so that the specimen could be exchanged easily, and the microbeam optics could be positioned close to the specimen. The cryochamber was oriented so that the specimen was positioned at its downstream end to enable wide-angle recordings (Fig. 1*a*).

2.4. X-ray diffraction recordings

2.4.1. Recordings of small-angle diffraction patterns. Diffraction/scattering recordings were carried out at the BL40XU beamline of SPring-8 as described previously (Iwamoto *et al.*, 2005, 2006). The small-angle diffraction patterns were recorded with a cooled CCD camera (Hamamatsu, C4880) with an image intensifier (Hamamatsu, V5445P-mod) placed downstream of a vacuum beam path. The specimen-to-detector distance was $\sim$3.2 m. The energy of the X-ray beams was 12.4 keV (λ = 0.1 nm), and the full flux was 10^{15} photons s^{-1}. The beam was attenuated to 1/100 by a fast-rotating shutter and, with the 2 µm defining pinhole as described below, 3×10^{10} photons reach the specimen per second (a flux density of $\sim 10^{16}$ photons s^{-1} mm^{-2}).

2.4.2. Recordings of wide-angle diffraction/scattering profiles. A wide-angle diffraction/scattering (WAXS) profile of ice was recorded on an imaging plate (BAS-SR, Fuji Film; size: 20 × 25 cm), which had a hole in the center to let the small-angle signal pass to the CCD detector, and could be rotated by a stepping-motor-driven mechanical stage. The specimen-to-detector distance was 175 mm. In front of the imaging plate was placed a brass plate, which had a keyhole-shaped opening [a circular opening for small-angle diffraction recording combined with a fan-shaped opening (angle 30°) to enable up to 12 wide-angle scattering profiles to be recorded on a single plate] (Fig. 1*b*). The imaging plate was read by a BAS 2500 reader (Fuji Film) with a pixel size of 100 × 100 µm.

2.5. Microbeam optics

The microbeam optics were basically the same as those used in the previous studies (Iwamoto *et al.*, 2005, 2006, 2007), and consisted of a defining pinhole (2 µm) and a guard pinhole (20 µm) drilled into a tantalum substratum (custom-made by Lenox Laser). Because the pinholes must be positioned in a narrow space in front of the specimen, they were attached on top of super-invar tubes (diameters of 5 mm and 8 mm for the defining and guard pinholes, respectively) (Fig. 1*a*).

2.6. Protocol for recording

2.6.1. General procedure. The specimens were quick-frozen either in the absence or presence of various cryoprotectants [5, 10 and 20% (*v*/*v*) of 2-methyl 2,4-pentanediol (MPD; Hampton Research), 20% (*v*/*v*) of dimethyl sulfoxide (DMSO; Sigma-Aldrich), 20% (*v*/*v*) of glycerol or 20% (*w*/*v*) of sucrose]. For each specimen, diffraction patterns were recorded at the surface level (the level at which diffraction patterns started to appear as the specimen was vertically moved into the beam), and at levels 10, 20, 30 50, 100 and 150 µm from the surface. From each level, 12 small-angle diffraction patterns were recorded by horizontally shifting the specimen by 10 µm after each exposure. The exposure time for recording a single small-angle diffraction pattern was 300 ms, but the shutter was kept open for 6 s to sufficiently expose the imaging plate. After exposures at each level, the imaging plate was rotated by 30° (thus the total exposure time for a single plate angle is 6 × 12 = 72 s). Data were processed by software built in-house. The background of WAXS scattering was fitted with a double-exponential decay function in the region where ice reflections were absent, and was subtracted from the whole scattering profile. This curve fitting was carried out using a commercial software package (*Prism*, Graphpad Inc.).

2.6.2. Assessment of radiation damage. The extent of radiation damage of the specimen and the effect of prolonged X-ray exposure on possible local temperature rise and resultant ice de-vitrification were assessed by continually irradiating a single spot of the specimen for a period of 700 s. A SAXS pattern was recorded every 10 s, while the imaging plate was rotated by 30° after each 100 s exposure.

3. Results

3.1. Measurement of cooling rate

The time course of the change of specimen temperature during plunge-freezing was estimated by placing a thermocouple junction on top of the plunging rod of the quick-freezing apparatus. The time course of the cooling, as shown in Fig. 2, consists of a slowly cooling phase above the freezing temperature followed by a rapidly cooling phase (Fig. 2*a*). The slow phase is considered to represent the phase in which the junction passes through the cool nitrogen gas above the liquid

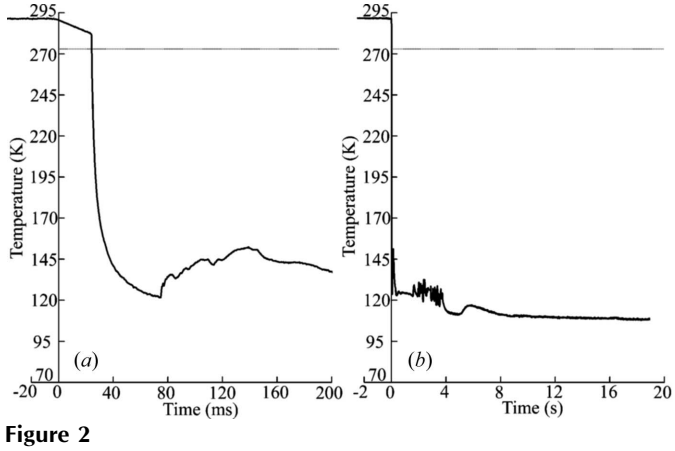

Figure 2
Cooling curves during and after plunging into liquid propane (99 K; this is slightly higher than the actual temperature used for freezing muscle specimens) as measured by using a fine-gauge thermocouple. (*a*) Fast time base; (*b*) slow time base. The time when the thermocouple enters the cold nitrogen gas is set to zero.

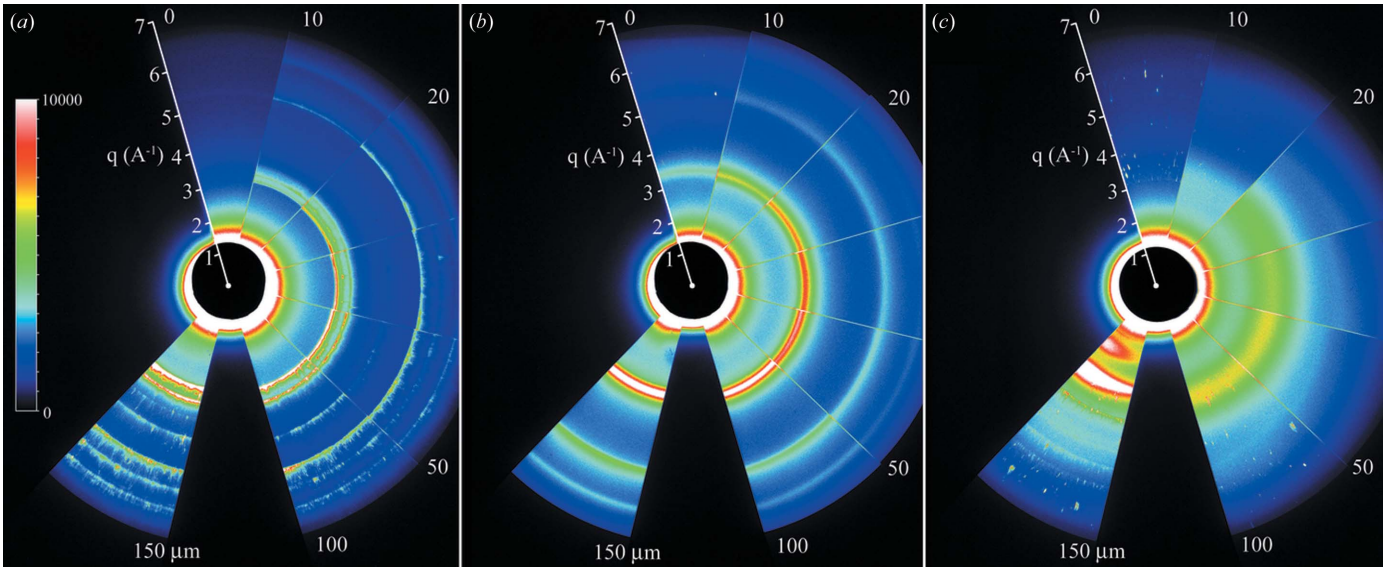

Figure 3
Examples of WAXS patterns from ice. (*a*) Sample frozen without a cryoprotectant; (*b*) sample frozen in the presence of 20% sucrose; (*c*) sample frozen in the presence of 20% MPD. The WAXS patterns cover the *q*-range between ~1.5 and ~7 Å^{-1}. The fan-shaped areas of exposure (30° each) represent the specimen depths of 0, 10, 20, 30, 50, 100 and 150 µm from the surface (from the top 0:00 position, clockwise). The 6:00 position was deliberately skipped to avoid confusion. In several cases the thickness of the specimen was less than 150 µm, and scattering considered to have come from the paper (on which the specimen was mounted) was recorded at this depth [the white-saturated area in (*c*)].

propane. The rate of cooling in the rapid phase, considered to represent the movement through the liquid propane, is very quick initially and is gradually decelerated. This rapid phase is further followed by a transient reversal of temperature to or slightly above the vitreous–crystalline transition temperature, but this reversal does not seem to cause de-vitrification as will be shown below. After this transient, the temperature slowly approaches the final temperature of liquid propane (Fig. 2*b*). The maximal rate of cooling was $(3.70 \pm 0.11) \times 10^4$ K s^{-1} (mean $\pm$ standard deviation, $n = 5$), and this value is much greater than the typical values for flash-cooling in protein crystallography (200–2000 K s^{-1}; Kriminski *et al.*, 2002).

3.2. Diffraction/scattering patterns in the presence or absence of various cryoprotectants

Examples of wide-angle scattering patterns of ice and a gallery of concomitantly recorded small-angle diffraction patterns from myofibrils are shown in Figs. 3 and 4, respectively. In Figs. 3(*a*) and 4(*a*) the specimen was quick-frozen in the absence of cryoprotectant. Fig. 3(*a*) shows the wide-angle recording by imaging plate, with each fan-shaped area (30°) showing the scattering pattern from each level of depth from the specimen surface. Except for the surface level, sharp peaks of ice crystals are observed. The innermost set of ice reflections, centered at a *d*-spacing of 3.7 Å, is divided into three peaks (3.90, 3.71 and 3.49 Å; see also the profiles in Fig. 5*a*), and this feature is characteristic of the phase of hexagonal ice (Murray *et al.*, 2005; Berejnov *et al.*, 2006). Sharp peaks are also observed at wider angles, including the one at a *d*-spacing of 2.24 Å. These peaks are also discrete along the circumference, indicating that the sizes of single ice crystals are not negligible when compared with the beam size (~2 µm).

Fig. 4(*a*) shows a gallery of small-angle diffraction patterns recorded at the same time. The hexagonally arranged reflection spots characteristic of the hexagonal lattices of myofilaments (Iwamoto *et al.*, 2002, 2006, 2007) are observed only at levels close to the surface (0 and 10 µm), and no reflections are observed at levels deeper than 10 µm. Typically, the pattern from the hexagonal lattice consists of intense 1,0 and 2,0 and weaker 1,1 and higher-order reflections originating from the filament lattice with a unit-cell size of ~45 nm (see Fig. 1*b*).

The scattering and diffraction patterns shown in Figs. 3(*b*) and 4(*b*) were recorded from the specimen frozen in the presence of 20% sucrose. The peak of ice at a *d*-spacing of 3.7 Å (Fig. 3*b*) is not divided into three, but is relatively sharp. The relative intensity of the peak at a *d*-spacing of ~2.24 Å increases with increasing depths when compared with that at 3.7 Å (see Fig. 5*b*). The diffuse peak at 1.85 Å also becomes more prominent with increasing depths (the outermost ring in Fig. 3*b*, out of the range of Fig. 5*b*). The positions of the three solitary peaks approximate those of the 111, 220 and 311 reflections of cubic ice (see Kohl *et al.*, 2000), and the observed features agree with those of a cubic-ice/vitreous-ice mixture as described by Berejnov *et al.* (2006). The intensities of the peaks are fairly uniform along the circumference, indicating that the sizes of single ice crystals (if present) are negligibly small when compared with the beam size.

In small-angle diffraction patterns, reflections from the hexagonal lattice of myofilaments are observed at all levels (Fig. 4*b*). Sharp reflections are observed at levels close to the surface, but the sharpness seems to be gradually lost as the

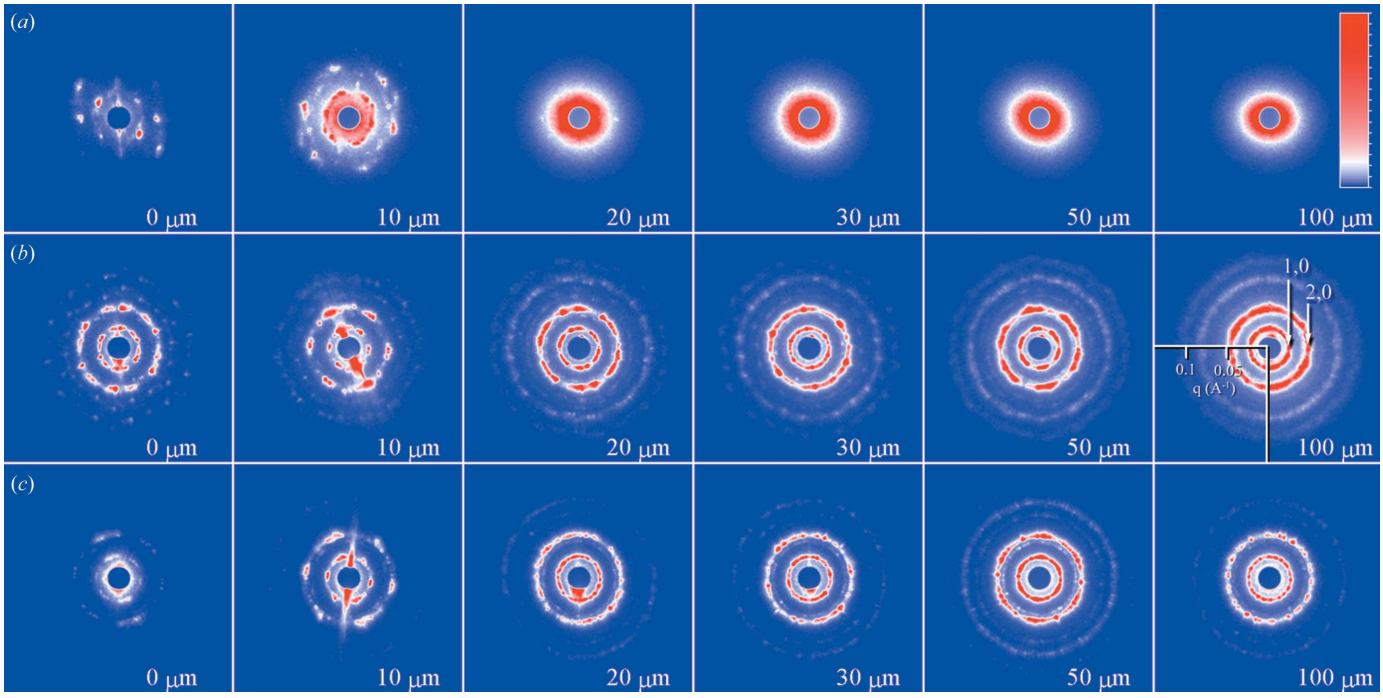

Figure 4
Examples of SAXS patterns from frozen myofibrils, simultaneously recorded with the WAXS patterns in Fig. 3. The reflections originate from the hexagonal lattice of myofilaments (see Fig. 1*b*). (*a*) Sample frozen without a cryoprotectant; (*b*) sample frozen in the presence of 20% sucrose; (*c*) sample frozen in the presence of 20% MPD. The SAXS patterns cover the q-range up to 0.15 Å^{-1} here. One representative diffraction pattern is shown out of the 12 patterns recorded at each depth (the depth is indicated at the bottom right of each pattern). Whether a diffraction pattern shows a feature of a single hexagonal filament lattice [as in the 0 μm pattern in (*b*)] depends on the orientation and straightness of myofibrils in the muscle fiber, rather than the goodness of freezing. Note that, in 20% MPD, the reflection spots are finely defined even at 100 μm (*c*) while in 20% sucrose the reflection spots are blurred (*b*). The color scale is logarithmic.

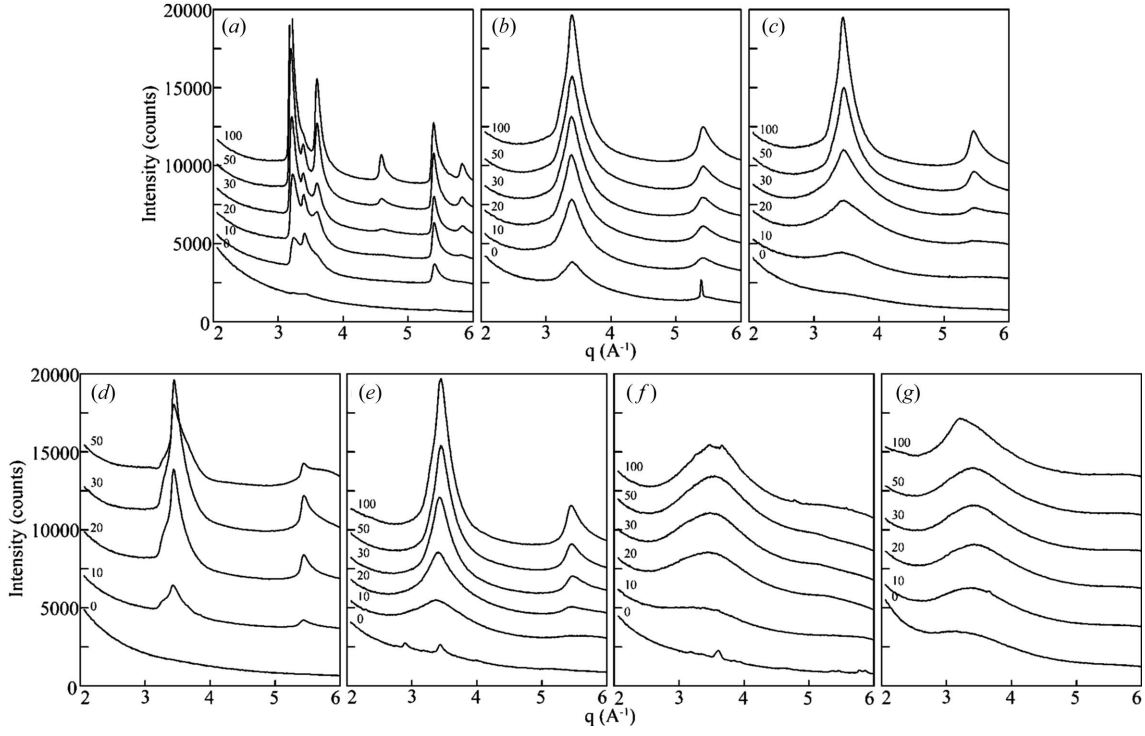

Figure 5
Integrated scattering intensity profiles from ice from the specimens frozen in the presence or absence of various cryoprotectants, taken from the WAXS recording as shown in Fig. 3. (*a*) Without cryoprotectant; (*b*) 20% sucrose; (*c*) 20% glycerol; (*d*) 5% MPD; (*e*) 10% MPD; (*f*) 20% MPD; (*g*) 20% DMSO. The baselines of the profiles from different depths (indicated on the left in μm) are offset for clarity. The small spikes in (*f*) originate from the sporadic reflections from ice crystals probably generated in the process of specimen trimming after freezing.

depth increases. The preservation of the reflections suggests that the state of the cubic–vitreous mixture is not very destructive for the macroscopic structure (small-angle regime) of this non-crystalline biological specimen. The inclusion of 20% glycerol yielded very similar results (patterns not shown; for profiles, see Fig. 5*c*).

Figs. 3(*c*) and 4(*c*) show the case of the specimen frozen in the presence of 20% MPD. In the scattering pattern from ice (Fig. 3*c*), the peak at a *d*-spacing of 3.7 Å remains very broad throughout the specimen (see also Fig. 3*f*), except for a small number of isolated sharp reflections from crystalline ice, which may have been formed or contaminated in the process of sample trimming. The reflections from the myofilament lattice in the small-angle diffraction patterns also remain sharp, and their details do not blur with depth, unlike in 20% sucrose (Fig. 4*c*). The inclusion of 20% DMSO also yielded good freezing and preservation of structure (patterns not shown; for profiles, see Fig. 5*g*).

Inclusion of lower concentrations of MPD resulted in unsatisfactory freezing qualities. With 5% MPD, the ice peak at 3.7 Å started to split (Fig. 5*d*), and the scattering profile of ice with 10% MPD (Fig. 5*e*) was similar to that with 20% sucrose or glycerol (see Figs. 5*b* and 5*c*). The quality of small-angle diffraction patterns reflected the state of the ice (not shown).

3.3. Relation between the specimen depth and the width of the ice peak

As has been reported in the previous study (Berejnov *et al.*, 2006) and confirmed in the present study, there is a tendency that the peak of scattering from ice at a *d*-spacing of 3.7 Å becomes sharper as the ice is gradually transformed from the vitreous to crystalline state. To describe this transition more quantitatively, the full width at half-maximum (FWHM) of the peak at 3.7 Å was determined from the wide-angle scattering profiles (Fig. 5) after subtracting the continuous background scattering.

In Fig. 6, the FWHM values determined in this way are plotted against the depth of the specimen from the surface. In the presence of 20% MPD or DMSO, the FWHM is $\sim$1.0 Å^{-1} in *q*-value and only slowly decreases with increasing depth. In the presence of 20% glycerol or 10% MPD, the FWHM is $\sim$0.8 Å^{-1} in *q*-value near the surface but it precipitously decreases with increasing depth and seems to converge at a level of 0.3–0.4 Å^{-1}. This feature is shared by 20% sucrose. These two levels of FWHM ($\sim$1.0 and 0.3–0.4 Å^{-1} in *q*-value) may represent two metastable states of ice below the vitreous–crystalline transition temperature.

3.4. Assessment of radiation damage

To assess the rate at which radiation damage develops in frozen samples, a single spot of a flight muscle specimen was continually exposed to a 2 µm microbeam for 700 s. The specimen was frozen in the presence of 20% MPD. During this period of exposure, the hexagonal filament lattice feature was gradually lost in the small-angle patterns because of the spread of each reflection spot (Fig. 7*a*). This change may be compared with the 'increased mosaicity' in protein crystals. The integrated intensity of the 2,0 reflection and intensity variation along the circumference also declined gradually (Fig. 7*b*).

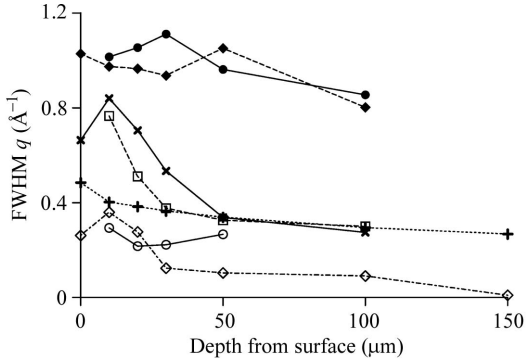

Figure 6
FWHM of the peak at a *d*-spacing of 3.7 Å (the 111 reflection of cubic ice) in the wide-angle scattering profile. Open diamonds, no cryoprotectant; plus signs, 20% sucrose; times signs, 20% glycerol; open circles, 5% MPD; open squares, 10% MPD; filled circles, 20% MPD; filled diamonds, 20% DMSO. The profiles were taken from Fig. 5 after subtraction of the background, which was fitted to a double-exponential decaying function. The FWHM in the absence of cryoprotectant was not determined accurately because of the multi-peaked nature.

These alterations were not due to the local heating of the specimen above the vitreous–crystalline transition temperature, as is evidenced by the concomitant WAXS measurement; the diffuse scattering centered at a *d*-spacing of 3.7 Å stayed broad throughout the 700 s period, indicating that the ideal vitreous state was maintained (Fig. 8; see also Appendix *A*). Thus, the result indicates that radiation damage develops even in samples in vitreous ice, but it occurs much more slowly than in unfrozen hydrated specimens. In unfrozen specimens, radiation damage occurs in seconds in a conventional undulator-based beamline (flux density, 3–4 $\times$ 10^{12} photons s^{-1} mm^{-2}). Since the flux density of the microbeam used here is several orders of magnitude greater than this, the protection provided by quick-freezing is remarkable. This confirms the conclusion of an earlier paper by Iwamoto *et al.* (2005).

4. Discussion

The present study has provided information about the relation between the depth from the surface, the conditions of the ice and of the sample structure itself, by performing simultaneous SAXS/WAXS recordings of quick-frozen biological specimens. The use of X-ray microbeams enabled recordings with high spatial resolution, revealing the local difference in the state of the ice and the extent of structure preservation. The present study was intended for non-crystalline hydrated biological specimens, but the information obtained here is also expected to be useful in protein crystallography and electron microscopic studies.

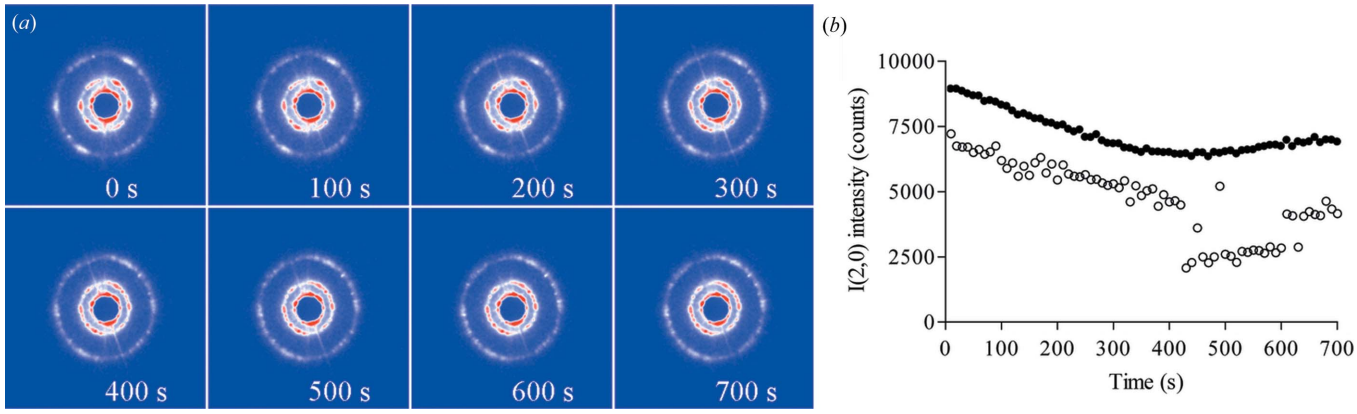

Figure 7
Assessment of radiation damage. (*a*) A series of SAXS patterns recorded from a single spot of sample while it was irradiated continually for 700 s. The cumulative exposure time is indicated at the bottom of each pattern. Note that the initially clear feature of the hexagonal lattice is gradually lost. These patterns were obtained from a flight muscle fiber from a giant cranefly, *Ctenacroscelis mikado*. (*b*) The time course of the change of integrated intensity of the 2,0 reflection (open circles) and its intensity variation along its circumference expressed as standard deviation (filled circles, its full scale is 0.7 of the averaged intensity). The sudden drop of intensity after 400 s and its sudden recovery after 600 s may be due to beam instability.

4.1. Relation between ice state and diffraction quality

In the present study the patterns of scattering from ice and of the small-angle diffraction from the sample were collected from narrow depths of the specimens, where the state of the ice was expected to be uniform. By using this strategy, the following has been shown. (i) All the reflections from the myofilament lattice are wiped out whenever hexagonal ice is formed, indicating that massive destruction of structure takes place. This is in marked contrast to protein crystals, in which many reflection spots from the protein lattice survive (*e.g.* Fig. 10 of Garman & Schneider, 1997). (ii) The best-preserved reflections from the myofilament lattice are observed in vitreous ice as expected. (iii) The structure of the specimen is fairly well preserved in the vitreous–cubic mixture state of ice, although the reflections from the myofilament lattice are somewhat blurred. The destruction of structure by hexagonal ice may be caused by volume expansion of the ice (Garman & Schneider, 1997) as well as by the growth of relatively large individual ice crystals (with the current beam size of 2 µm, reflections from individual single ice crystals can be recognized; see Fig. 3*a*). The size of individual ice crystals could be comparable with or greater than the unit-cell size of the myofilament lattices.

In the vitreous–cubic mixture, the reflections from individual ice crystals were not recognized even with the current beam size (the ice reflections have an appearance of Debye–Scherrer rings of uniform intensities; see Fig. 3*b*). Possibly the ice crystals are smaller than the unit cell of myofilament lattices, leaving the small-angle reflections fairly intact. However, the structure of constituent proteins may be affected by cubic ice crystals. The failure to detect reflection spots from individual cubic ice crystals may be because there were simply too many reflection spots (although the beam size was 2 µm, the specimen was several hundred micrometers long along the beam axis, allowing an enormous number of ice crystals to be present in the beam path), or alternatively

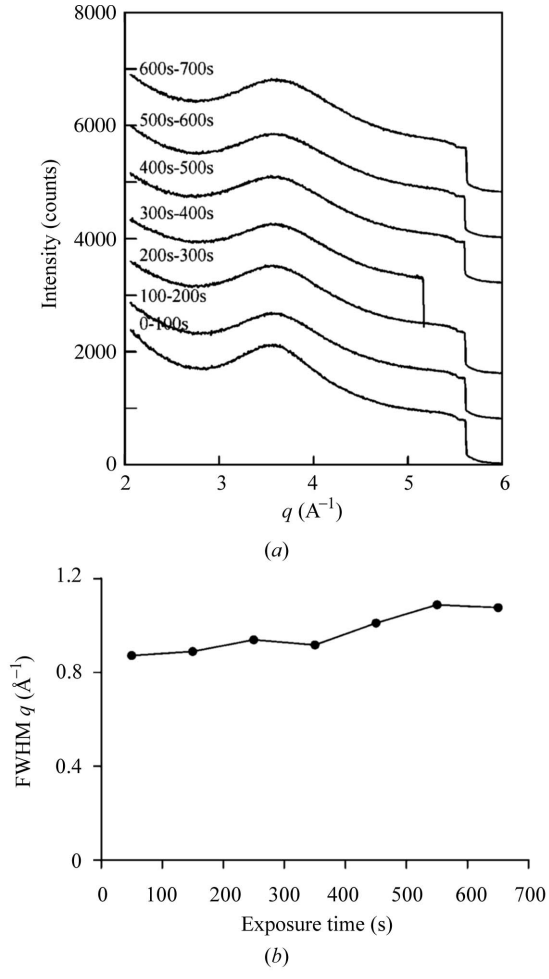

Figure 8
WAXS recordings of scattering from ice simultaneously recorded with the SAXS patterns in Fig. 7. (*a*) WAXS profiles recorded from 100 s segments of the continuous 700 s exposure. Note that the scattering remains diffuse throughout the period, indicating that the ice remained vitreous. (*b*) FWHM of the ice peak in (*a*).

because of the wide peaks of the Laue function owing to the limited number of unit cells in each crystal. The size of the cubic ice crystals may be estimated in future studies if much smaller frozen specimens are used (*i.e.* fewer ice crystals in the beam path) in combination with microdiffraction techniques.

4.2. Choice and concentration of cryoprotectants

The major interest in diffraction recordings from non-crystalline biological samples, especially large-scale functional assemblies of proteins/enzymes like muscle, is to freeze and observe their structures at desired moments of their functions. Certainly, cryoprotectants prevent the structures from being destroyed by ice crystals, but their use should best be avoided because of their potential or real adverse effects on the structure and function of the protein complexes.

In our previous studies (Iwamoto *et al.*, 2006, 2007), MPD at a 20% concentration has been the cryoprotectant of choice, because of its ability to preserve small-angle reflections over a large depth of specimens. The good preservation of structure was confirmed in the present study, and the width of the scattering peak of vitreous ice narrowed only slightly at a depth of 100 µm from the surface (Fig. 6). Equally good preservation was observed for 20% DMSO. However, both of these solvents inhibit muscle contraction at this concentration (MPD: Iwamoto, unpublished; DMSO: Mariano *et al.*, 2001), and freezing of contracting muscle fibers, as is often done in electron microscopic studies (*e.g.* Hirose *et al.*, 1993), would be impossible in the presence of these solvents. MPD at concentrations lower than 20% was found inadequate for protection, and, at 5%, tolerable small-angle reflections were observed only at depths of 20 µm and smaller. The minimum concentrations required to vitrify flash-cooled droplets have been reported to be 15% for MPD and 28% for DMSO (Berejnov *et al.*, 2006).

The present study showed that, at a 20% concentration, glycerol and sucrose are inferior cryoprotectants than MPD or DMSO, creating a vitrified-ice/cubic-ice mixture in most of the depths. However, these solutes are superior to MPD and DMSO in preserving the contractility of muscle fibers (unpublished). Their vitrifying ability will probably be improved at higher concentrations [the minimum vitrifying concentrations have been reported by Berejnov *et al.* (2006) to be 28% and 36% for glycerol and sucrose, respectively]. However, raising the concentration of these solutes by more than 20% may not be a good idea, because they will increase the electron density of the medium and consequently decrease the contrast of proteins. For proteins with average densities, their densities match that of the medium at 50–60% sucrose, and no reflection will be generated from the specimen at this sucrose concentration.

To summarize, both groups of cryoprotectants have merits and demerits, and at present one should select one of them depending on the purpose of the experiments. The cooling should be made as fast as possible, by plunging into liquid propane or slush-cooled liquid nitrogen, which has been shown to be equally effective (Reedy *et al.*, 2008). The concentration of the cryoprotectant should be kept minimal, especially in physiology-oriented studies. In this case, microdiffraction from the surface area will be beneficial.

4.3. Effect of impact on the structure of specimens

In the present study, uncovered wet specimens were directly plunged into liquid propane. By doing so, the water layer on the surface can be minimized, ensuring efficient heat transfer. However, this poses a risk of deforming soft materials on impact. The means for protecting the specimens from such deformation include the use of protective sheaths such as thin-walled glass capillaries, and, in the case of organelles suspended in solution, the use of protective sheaths is indispensable. Actually, thin-walled glass capillaries have been used for the flight muscle fibers of fruit flies (Iwamoto *et al.*, 2007), which were still developing in the pupal stage and were therefore very fragile. The expected problems with the use of such protective sheaths are that (i) the sheaths themselves reduce the efficiency of heat conduction and that (ii) a volume of water is confined within a space between the specimen and the sheath, and this water further reduces the efficiency of heat conduction. The effect of the use of protective sheaths may also be evaluated by means of microbeam SAXS/WAXS measurement as employed in the present study.

4.4. Implications for electron microscopy

In electron microscopy of frozen-substituted specimens, the regions of good and poor preservation are usually obvious at a glance of the electron micrographs, and it is assumed that the ice in the region of good preservation is vitreous. However, the present study showed that ice in the vitreous–cubic mixture state yields some extent of preservation, and the correlation of this state in the quality of electron micrographs is unknown. Direct correlation between electron micrographs and ice qualities is possible by electron diffraction (Sartori *et al.*, 1996), but this requires cryosections of specimens. The high penetrability and spatial resolution provided by X-ray microbeams will also be useful in evaluating the freezing method for cryoelectron microscopy, because the frozen specimens scanned by X-ray beams can be retrieved for freeze-substitution.

4.5. Non-crystalline biological specimens *versus* protein crystals

Most of the published evaluation studies for cryodiffraction have been intended for protein crystallography. Although a large part of information obtained through these and the present studies may be applicable to both non-crystalline and crystalline specimens, there seem to be several differences in these specimens as regards to the responses to cryogenic procedures.

In protein crystals, reflections from the protein lattice remain observable in the presence of hexagonal ice; it is the increased mosaic spread of the crystal that causes a problem (Garman & Schneider, 1997; Kriminski *et al.*, 2002). In another case, problems arise because of the loss of available reflection

spots from the protein lattice as they are masked by the intense diffraction from the ice (*e.g.* Fisher *et al.*, 2008). In general, protein crystals seem to be more tolerable to ice crystal formation than non-crystalline specimens; for most crystals, flash-cooling in a gas stream is perfectly adequate (Garman & Schneider, 1997), and even 'annealing' of the crystals by temporarily warming them up (even to a melting temperature) often helps in reducing mosaicity (Kriminski *et al.*, 2002).

In non-crystalline biological specimens the formation of hexagonal ice eliminates small-angle reflection spots from the specimen altogether. Rapid cooling in a medium with a large melting–boiling temperature difference (such as propane) seems to be pre-requisite. All these differences may come from the differences in the water content of protein crystals and non-crystalline materials. For example, the tetragonal and triclinic crystal forms of lysozyme contain ∼42 and ∼26% (*w*/*w*) of water, respectively (Kriminski *et al.*, 2002), whereas myofibrils of muscle as used here contain as much as ∼86% (*w*/*w*) of water (calculated from data by Yates *et al.*, 1983). The rate of cooling required to vitrify a droplet of pure water is five to six orders of magnitude greater than required for a hydrated powder of lysozyme containing 23–38% of water (Kriminski *et al.*, 2002). Apparently, the dense packing of proteins in crystals serves as a cryoprotectant by itself. Since virus crystals and non-crystalline hydrated biological specimens other than muscle are expected to contain equally large amounts of water, the pursuit of techniques to vitrify these specimens without sacrificing their native structures and functions will be increasingly important in future structural biology. In the process of this pursuit, the evaluation of structure preservation by microbeam SAXS/WAXS measurement as presented here will certainly be one of the most powerful approaches to fulfill the purposes.

APPENDIX *A*
Assessment of temperature rise during microbeam irradiation

The measurements shown above indicate that X-ray microbeams with the photon flux used here do not heat up frozen specimens above the vitreous–crystalline transition temperature even after a 700 s period of exposure. However, it would be useful to estimate the extent of local temperature rise during exposure in the current geometry of specimen and heat sink (Fig. 1*d*) and also to estimate the safe limit of X-ray photon flux to keep the specimen below the vitreous–crystalline transition temperature.

It is considered that the local temperature of the irradiated area is determined by the balance between the photon energy absorbed by the specimen and the conduction of heat from the irradiated area to the heat sink cooled to 70 K.

The rate of energy absorption by the specimen is expressed as

$$Q_1 = fae, \tag{1}$$

where f is the photon flux (photons s^{-1}), a is the fraction of energy absorbed by the specimen, and e is the energy of a photon. The energy of a photon e is expressed as

$$e = hc/\lambda, \tag{2}$$

where h is Planck's constant, c is the speed of light and λ is the wavelength, which is 1.0 Å under current conditions. The photon flux f, as estimated from the measurement by using a PIN photodiode, was 3×10^{10} photons s^{-1}. The X-ray path-length in the specimen was 500 µm and, by assuming that the specimen has an electron density equal to that of water, a is expected to be 0.127 (Center for X-ray Optics; http://www-cxro.lbl.gov/), and Q_1 is calculated to be $\sim 7.4 \times 10^{-6}$ J s^{-1}.

On the other hand, the rate of heat conduction from the specimen to the heat sink, in this case a brass rod that is always kept at 70 K, is expressed as

$$Q_2 = kS\Delta T/L, \tag{3}$$

where k is the thermal conductivity, S is the area of surface through which heat is conducted, ΔT is the temperature of the specimen above that of the heat sink, and L is the distance between the irradiated volume of the specimen and the heat sink. We assume that half of the surface of the irradiated volume contributes to heat conduction (Fig. 1*d*), and in this case S is calculated to be 1.57×10^{-9} m^2. We further assume that L is 500 µm and the space between the irradiated volume and the heat sink is filled with ice with $k = 2.2$ W m^{-1} K. In a steady state, $Q_1 = Q_2$, and from this ΔT is calculated to be 1.07 K with the assumption that all the absorbed energy is converted to heat. Therefore, the temperature rise owing to microbeam irradiation is negligible with the current photon flux. Inclusion of cryoprotectant may increase X-ray absorption by the specimen, but with the current photon flux it is unlikely to affect the temperature rise in a significant manner.

The calculation shows that the temperature could rise above the transition temperature if an unattenuated microbeam (3×10^{12} photons s^{-1}) is used (from 70 K to ∼180 K). The safe limit of flux in the current settings (with a 2 µm microbeam) would be 10^{12} photons s^{-1} or below.

The author expresses his thanks to Dr N. Yagi for his support and discussion, and Dr T. Inoda for the reared specimen of *Lethocerus*. The study was conducted as an in-house research project at SPring-8 (proposal No. 2007B1883), and was supported in part by the X-ray Free Electron Laser Utilization Research Project of the Ministry of Education, Culture, Sports, Science and Technology of Japan (MEXT).

References

Barnard, T. (1987). *Scan. Microsc.* **1**, 1217–1224.
Berejnov, V., Husseini, N. S., Alsaied, O. A. & Thorne, R. E. (2006). *J. Appl. Cryst.* **39**, 244–251.
Fisher, S. J., Helliwell, J. R., Khurshid, S., Govada, L., Redwood, C., Squire, J. M. & Chayen, N. E. (2008). *Acta Cryst.* D**64**, 658–664.
Garman, E. F. & Schneider, T. R. (1997). *J. Appl. Cryst.* **30**, 211–237.
Hirose, K., Lenart, T. D., Franzini-Armstrong, C. & Goldman, Y. E. (1993). *Biophys. J.* **65**, 397–408.
Iwamoto, H. (1995). *Biophys. J.* **68**, 243–250.

Iwamoto, H. (2000). *Biophys. J.* **78**, 3138–3149.
Iwamoto, H., Inoue, K., Fujisawa, T. & Yagi, N. (2005). *J. Synchrotron Rad.* **12**, 479–483.
Iwamoto, H., Inoue, K., Matsuo, T. & Yagi, N. (2007). *Proc. R. Soc. London Ser. B*, **274**, 2297–2305.
Iwamoto, H., Inoue, K. & Yagi, N. (2006). *Proc. R. Soc. London Ser. B*, **273**, 677–685.
Iwamoto, H., Nishikawa, Y., Wakayama, J. & Fujisawa, T. (2002). *Biophys. J.* **83**, 1074–1081.
Kohl, I., Mayer, E. & Hallbrucker, A. (2000). *Phys. Chem. Chem. Phys.* **2**, 1579–1586.
Kriminski, S., Caylor, C. L., Nonato, M. C., Finkelstein, K. D. & Thorne, R. E. (2002). *Acta Cryst.* D**58**, 459–471.
Lepault, J., Bigot, D., Studer, D. & Erk, I. (1997). *J. Microsc.* **187**, 158–166.
Mariano, A. C., Alexandre, G. M. C., Silva, L. C., Romeiro, A., Cameron, L. C., Chen, Y., Chase, P. B. & Sorenson, M. M. (2001). *Biochem. J.* **358**, 627–636.
Murray, B. J., Knopf, D. A. & Bertram, A. K. (2005). *Nature (London)*, **434**, 202–205.
Reedy, M. K., Bekyarova, T. I., Lucaveche, C., Ward, A. B., Reedy, M. C., Pahl, R. & Irving, T. C. (2008). *Biophys. J.* **94** (Abst. Issue), 634.
Riekel, C. & Davies, R. J. (2005). *Curr. Opin. Colloid Interf. Sci.* **9**, 396–403.
Riekel, C., García Gutiérrez, M. C., Gourrier, A. & Roth, S. (2003). *Anal. Bioanal. Chem.* **376**, 594–601.
Sartori, N., Bednar, J. & Dubochet, J. (1996). *J. Microsc.* **182**, 163–168.
Tregear, R. T., Edwards, R. J., Irving, T. C., Poole, K. J. V., Reedy, M. C., Schmitz, H., Towns-Andrews, E. & Reedy, M. K. (1998). *Biophys. J.* **74**, 1439–1451.
Warkentin, M., Berejnov, V., Husseini, N. S. & Thorne, R. E. (2006). *J. Appl. Cryst.* **39**, 805–811.
Yates, L. D., Greaser, M. L. & Huxley, H. E. (1983). *J. Mol. Biol.* **168**, 123–141.